

Effects of plasma flow velocity on melt-layer splashing and erosion during plasma instabilities

G. Miloshevsky and A. Hassanein

Center for Materials under Extreme Environment, School of Nuclear Engineering,
Purdue University, West Lafayette, IN 47907, USA

E-mail: gennady@purdue.edu

Received 5 November 2013, revised 14 January 2014

Accepted for publication 14 January 2014

Published 21 February 2014

Abstract

It is recognized both experimentally and computationally that the main damage of divertor in fusion devices such as ITER could be due to melting of metallic plasma facing components such as tungsten developed during plasma instabilities. Macroscopic melt motion and splashing with ejection of molten droplets into plasma are major concern. The computational modelling of uncoupled/coupled plasma–melt flows is carried out using the developed VoF-MHD model. The goal of this research is to study the effect of viscous plasma flowing with a velocity of $0\text{--}5\text{ km s}^{-1}$ on the melt stability. Development of running waves with large wavelengths is observed on the melt surface in the absence of plasma impact. The magnetic field of 5 T that is parallel to the direction of melt motion completely damps these surface waves. When the magnetic field is perpendicular to the direction of melt motion, the small-amplitude standing waves are formed. The viscous plasma streaming with $\sim 0.1\text{--}5\text{ km s}^{-1}$ over the melt surface develops waves that are not damped by the magnetic field which is either parallel or normal to the direction of melt motion. It is observed that the surface waves are generated much faster at higher plasma speeds and their wavelength decreases accordingly. The high-speed viscous plasma flowing with $\sim 5\text{ km s}^{-1}$ produces small melt ripples that break up into droplets carried away by the plasma wind. This is a major concern for magnetic fusion as a reliable source of energy production.

Keywords: plasma facing components, plasma flow, melt layer, splashing, droplets

(Some figures may appear in colour only in the online journal)

1. Introduction

Under off-normal transient events such as the edge localized modes (ELMs) or plasma disruptions [1, 2], the high thermal energy can be deposited on localized areas of plasma-facing components (PFC) in fusion devices [3, 4]. Among high-Z materials, pure tungsten (W) demonstrates the highest resistance against thermal loads under plasma disruption conditions. It has high thermal conductivity, high melting point and low sputtering [5]. It has been evaluated as a plasma-facing material for divertor plates in steady-state magnetic fusion devices [6]. However, a critical problem with W is melting under intense thermal loads, melt-layer formation, melt motion and splashing with ejection of melt droplets into a plasma [7–15]. This leads to plasma contamination by high-Z material and significant damage of PFCs. Therefore, it is important to understand the physical mechanisms of macroscopic melt splashing and losses and possible ways of their mitigation.

Melt motion and droplet ejection has been observed in the experiments carried out in TEXTOR tokamak [16–18], numerous plasma guns [19–29] and electron beam facilities

[30]. Up to date, the W exposures to a hot plasma in the tokamaks have simulated steady-state deep melting, although the transient melt exposures have been performed at JET in 2013. The JET results are subject to future publications. The plasma gun devices have also been used to study the transient shallow melting. Shallow melting is of particular interest for ITER and future reactors, since ELMs and disruptions are the most likely candidates for melting the surfaces. The disruption conditions in tokamaks cannot be always reproduced using the simulation devices. Although the relevant energy density can be achieved, other parameters such as pulse duration and particle energy can considerably differ in various devices [31]. Many facilities do not include the effects of a magnetic field. Therefore, the results of experimental studies in simulation devices should be carefully interpreted. Fine spray of W-melt is observed in recent TEXTOR experiments and was constantly present having W-melt macroscopic losses as splashes with continuous ligaments and large droplets [32–34]. The emission of fine melt spray was attributed to melt boiling with bubble bursting [35], while melt splashes with droplets are due to the development of Kelvin–Helmholtz instability [36].

The main theoretical approaches used to study the melt motion and splashing are the linear stability analysis [13, 14, 37, 38] and computational modelling [12, 36, 38–40]. The conditions for development and growth of surface waves at the plasma–melt interface were predicted using the inviscid stability analysis [36, 37, 40]. In agreement with these predictions, the growth of surface disturbances and their transformation into long W-melt ligaments that disintegrated into liquid droplets was observed using comprehensive modelling [36, 40]. The inviscid stability analysis [36, 37] was further extended to include the effects of viscosity, heat transfer and mass exchange across the interface [38]. It is found that plasma viscosity has a destabilizing effect on melt layer. The surface waves with fastest growing rate have shifted toward shorter wavelengths with the critical velocity is considerably reduced. However, in this viscous stability analysis the short-length waves were stabilized by heat and mass transfer across the melt interface. The computational model [38] that includes heat transfer and vaporization effects was also developed implementing the open-source OpenFoam libraries [41]. The development of short waves with fine melt droplets stripped from wave tips and dragged away by the plasma flow is observed in the absence of melt evaporation. In the presence of phase change at the interface, it is found that unstable waves are suppressed due to melt evaporation [38].

In this work, the volume of fluid (VoF) model [42, 43] is coupled with magnetohydrodynamic (MHD) model [44] in order to investigate the behaviour of W-melt flow on a substrate, melt-layer motion, splashing and droplet ejection under ITER-relevant conditions. The melt motion is studied in the absence and the presence of coupling to the plasma flow, and without/with the effects of a magnetic field. The motion of melt with a velocity of $\sim 1.7 \text{ m s}^{-1}$ was observed in TEXTOR experiments [45]. Therefore, we use the velocity of W-melt $\sim 2 \text{ m s}^{-1}$. The plasma flow velocity is uncertain. During ELMs in the DIII-D tokamak, the ELM plasma velocity is found to be $\sim 0.5 \text{ km s}^{-1}$ in the poloidal direction and $\sim 10\text{--}20 \text{ km s}^{-1}$ in the toroidal direction [46]. Higher plasma speeds are expected during plasma disruptions. Plasma gun compressors and accelerators can generate plasma streams with speeds higher than $\sim 100\text{--}400 \text{ km s}^{-1}$ [47, 48]. Therefore, the main purpose of this study is to investigate how the viscous plasma with increasing speed from 0 km s^{-1} to 5 km s^{-1} induces the development of waves on the melt surface, their growth, melt splashing and ejection of molten droplets. The VoF fractions of melt and plasma, the distributions of pressure, velocity and magnetic field are reported.

2. Mathematical model and computational methods

The mathematical model is developed to treat the flow of liquid metal with free surface as well as the coupled flow of two fluids (plasma and liquid metal) under the influence of an external magnetic field. The model is based on a VoF approach [42, 43] implemented within the OpenFOAM (Open Field Operation and Manipulation) toolbox [41], a free open-source CFD software package. OpenFOAM combines C++ libraries for different mathematical, numerical and physical models. Various solvers and utilities can be created by combining these standard numerical tools with the physics

models available in OpenFOAM. Moreover, custom solvers and new physics models can be developed and implemented for solving specific problems. Therefore, the OpenFOAM framework opens possibilities to develop new physics and computational models. As a starting point, we have utilized the VoF solver named interFoam [49]. The performance of this two-fluid solver was recently evaluated for a variety of validation test cases [50]. We have implemented the effects of thermal conduction and magnetic field in the algorithm of interFoam. The VoF-MHD model was benchmarked against the Shercliff and Hunts problems of liquid metal flow in a rectangular duct under the influence of an externally applied magnetic field [51, 52]. It is observed that with the increasing magnetic field, the velocity of liquid metal decreases and its velocity profile becomes flat in the duct core with thin Hartmann boundary layers at the duct walls. The numerical velocity profiles are found in a very good agreement with analytical solutions. The evolution of a single bubble rising in a liquid and undergoing shape deformations is also investigated. The results are found in a reasonable agreement with those reported in [53]. Modelling of a single bubble rising in a liquid metal under imposed vertical magnetic field are also performed. In agreement with previous simulation results [54], the bubble elongation in the direction of a magnetic field and the reduction of terminal bubble velocity are found for large Hartmann numbers.

The governing equations for unsteady, incompressible, immiscible two-fluid flow with heat transfer include the continuity, momentum, energy and volume fraction equations. They can be written as

$$\nabla \cdot \vec{u} = 0, \quad (1)$$

$$\frac{\partial \rho \vec{u}}{\partial t} + \nabla \cdot (\rho \vec{u} \vec{u}) = -\nabla p + 2\nabla \cdot (\mu \hat{\tau}) + \gamma \kappa \nabla \alpha_m + \rho \vec{g} + \vec{J} \times \vec{B}, \quad (2)$$

$$\frac{\partial \rho c_p T}{\partial t} + \nabla \cdot (\rho c_p \vec{u} T) = \nabla \cdot (k \nabla T) + q, \quad (3)$$

$$\frac{\partial \alpha_m}{\partial t} + \nabla \cdot (\alpha_m \vec{u}) + \nabla \cdot (\alpha_m (1 - \alpha_m) \vec{u}_c) = 0, \quad (4)$$

where \vec{u} is the velocity field. In equation (2), $\rho = \alpha_m \rho_m + \alpha_p \rho_p$ is the density field with values of ρ_m and ρ_p for melt and plasma fluids, α_m is the volume fraction of melt, $\alpha_p = 1 - \alpha_m$ is the volume fraction of plasma, p is the pressure field, $\mu = \alpha_m \mu_m + \alpha_p \mu_p$ is the viscosity with components of μ_m and μ_p for melt and plasma fluids, $\hat{\tau} = (\nabla \vec{u} + (\nabla \vec{u})^T)/2$ is the viscous stress tensor, γ is the surface tension of melt, $\kappa = -\nabla \cdot (\nabla \alpha_m / |\nabla \alpha_m|)$ is the curvature of the interface, \vec{g} is the acceleration due to gravity, \vec{B} is the magnetic field and \vec{J} represents the current density. In equation (3), T is the temperature field, $c_p = \alpha_m c_{pm} + \alpha_p c_{pp}$ and $k = \alpha_m k_m + \alpha_p k_p$ are, respectively, the specific heat capacity at constant pressure and the thermal conductivity assuming the values c_{pm} , k_m and c_{pp} , k_p for melt and plasma fluids, $q = \vec{J} \cdot \vec{J} / \sigma$ is the Joule heating due to the electric current, $\sigma = \alpha_m \sigma_m + \alpha_p \sigma_p$ is the electric conductivity with values of σ_m and σ_p for melt and plasma fluids. In equation (4), \vec{u}_c is the compression velocity, which is included for artificial interface compression [43, 55]. This extra compression contributes only in the interfacial region providing sharp interface and ensuring that

α_m is limited between 0 and 1. Single velocity, pressure, temperature and magnetic fields are defined for plasma and melt fluids. Densities, volume fractions, viscosities, specific heat capacities, thermal and electrical conductivities are defined separately for each of fluids. The plasma–melt interface is tracked using volume fractions.

We have implemented the heat conduction equation (3) into the basic VoF model (equations (1), (2) and (4)) available in interFoam. Equation (3) couples the velocity–temperature field. It also includes an additional source term q due to the Joule heating. In the momentum equation (2) we have included the vector product [44]

$$\vec{J} \times \vec{B} = -\nabla \frac{B^2}{2\mu} + \frac{\vec{B} \nabla \vec{B}}{\mu} \quad (5)$$

that describes the Lorentz force acting on the flow of electrically conducting fluids. In equation (5), μ is the magnetic permeability. The first term on the right-hand side of equation (5) describes the gradient of magnetic pressure. It can be combined with the gradient of hydrodynamic pressure in the momentum equation (2). The second term in equation (5) is the magnetic tension that acts to straighten the bent magnetic field lines. The magnetic induction equation describing the evolution of \vec{B} can be written as [44]

$$\frac{\partial \vec{B}}{\partial t} + \nabla \cdot (\vec{u} \vec{B} - \vec{B} \vec{u}) - \nabla \cdot \frac{\nabla \vec{B}}{\sigma \mu} = 0. \quad (6)$$

Using the magnetic field \vec{B} calculated from equation (6), the current density is then expressed as $\vec{J} = (\nabla \times \vec{B})/\mu$. The electric field \vec{E} can be determined from Ohm's law $\vec{J} = \sigma(\vec{E} + \vec{u} \times \vec{B})$. The calculated \vec{B} and \vec{J} are used in equations (2) and (3) to compute the Lorentz force and Joule heating. It should be noted that in the present model, the Lorentz force is caused by the induced current \vec{J} that is generated due to the melt motion and flow velocity variations. The induced electric field \vec{E} is produced by this induced current and an electromotive field $\vec{E}_{em} = -\vec{u} \times \vec{B}$. The external currents such as the thermoelectric current due to thermal electron emission are not currently implemented in the VoF-MHD model. This implementation requiring a modification of boundary conditions will be performed in future developments of this model.

The momentum equation (2) and magnetic induction equation (6) are written in the form that can be solved within the OpenFOAM framework. Therefore, the VoF-MHD solver for the modelling of liquid metal motion and splashing without/with the impact of plasma was developed and implemented using the OpenFoam library. The magnetic pressure and tension terms (equation (5)) actually describing the Lorentz force are introduced in the PISO loop [49, 56] for the pressure–velocity coupling in the Navier–Stokes equations (1) and (2). The induction equation (6) is solved separately as an additional transport equation using the B-PISO loop that is similar to the PISO loop for the pressure–velocity coupling. A fictitious magnetic flux is introduced into the induction equation (6) in order to facilitate the divergence-free constraint on the magnetic field, $\nabla \cdot \vec{B} = 0$. This flux has no physical meaning, and at reaching the convergence it represents a small discretization error. The multidimensional universal limiter with explicit solution (MULES) [49] is used to solve the volume fraction transport equation (4).

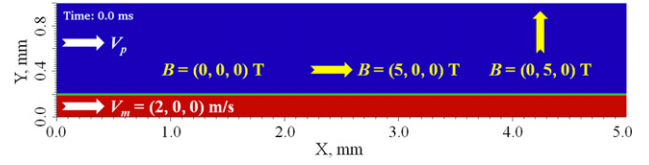


Figure 1. Sketch of the 2D computational domain used in simulations.

3. Results and discussion

In this section, we describe the numerical set-up of the problem, 2D computational domain, W-melt-plasma physical properties and parameters, and results on the motion of W-melt on a solid substrate without/with the impact of plasma. The modelling of plasma–melt flow is performed in 2D geometry, since the full 3D simulations require enormous computational resources.

3.1. Computational domain and numerical set-up

The 2D computational domain is sketched in figure 1. The size of computational domain is set to 5 mm in length and 1 mm in height. The interface between W-melt (in red) and plasma (in blue) is located at $Y = 200 \mu\text{m}$ (figure 1). The inlet and outlet of the computational domain are on the left and right sides, respectively.

The velocity of W-melt and plasma is prescribed at the inlet, and the boundary condition on the pressure is zero gradient. The fixed value is used for the pressure at the outlet, with zero gradient for velocity. The solid wall is located on the bottom. The non-slip boundary condition is used for velocity, with zero gradient for pressure. The top is a free boundary permitting both outflow and inflow of plasma. The parameters and physical properties of W-melt and plasma are as follows [38]. W-melt thickness is $\sim 200 \mu\text{m}$. The molten W is kept at temperature $T_m = 3695 \text{ K}$. W-melt density is $\rho_m = 16400 \text{ kg m}^{-3}$. The surface tension of W-melt is $\gamma = 2.48 \text{ N m}^{-1}$. The dynamic viscosity is $\mu_m \sim 7 \times 10^{-3} \text{ kg m}^{-1} \text{ s}^{-1}$. The specific heat capacity is $c_{pm} \sim 280 \text{ J kg}^{-1} \text{ K}^{-1}$. The heat conduction coefficient is $k_m \sim 80 \text{ W m}^{-1} \text{ K}^{-1}$. The electric conductivity is $\sigma_m \sim 6.9 \times 10^5 \Omega^{-1} \text{ m}^{-1}$. The above parameters are defined at the melting temperature of W-melt. The velocity of W-melt is set to $\sim 2 \text{ m s}^{-1}$. The velocity of hydrogen plasma streaming over the W-melt surface was in the range from 0 to 5000 m s^{-1} . The number density of plasma is $\sim 10^{20} \text{ m}^{-3}$ ($\rho_p \sim 1.67 \times 10^{-7} \text{ kg m}^{-3}$) that is relevant for ITER conditions. The plasma is held at the temperature of W-melt, $T_p = 3695 \text{ K}$. The dynamic viscosity is $10^{-5} \text{ kg m}^{-1} \text{ s}^{-1}$. The specific heat capacity was estimated using the ideal gas law as $c_{pp} = \chi R_p/(\chi - 1) \sim 2 \times 10^4 \text{ J kg}^{-1} \text{ K}^{-1}$, where $\chi = 5/3$ is the adiabatic constant of monatomic hydrogen plasma. The thermal conductivity due to electrons is estimated as $k_p \sim 4.4 \times 10^{-11} (T_p(\text{K}))^{5/2} (\ln \Lambda/10)^{-1} \sim 3.65 \times 10^{-2} \text{ W m}^{-1} \text{ K}^{-1}$, where $\ln \Lambda \sim 10$ is the Coulomb logarithm. The electrical conductivity is calculated using $\sigma_p \sim 1.5 \times 10^{-3} (T_p(\text{K}))^{3/2} (\ln \Lambda/10)^{-1} \sim 3.37 \times 10^2 \Omega^{-1} \text{ m}^{-1}$. The background pressure for the whole system is set to $p = 10^5 \text{ Pa}$. The applied magnetic field is $B = 5 \text{ T}$. The simulations are performed for three cases: (1) no magnetic field; (2) the

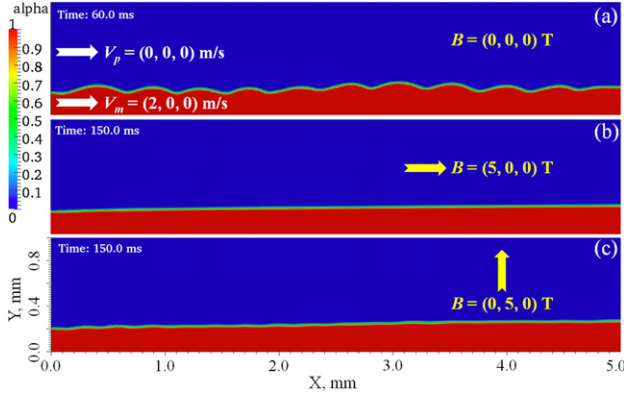


Figure 2. Volume fraction (alpha) of W-melt in the absence of plasma stream (a) without magnetic field, (b) with an externally applied magnetic field parallel to the flow direction of W-melt and (c) a magnetic field normal to the direction of W-melt flow. The velocity of W-melt is 2 m s^{-1} .

direction of magnetic field is aligned with the flow direction; and (3) the direction of magnetic field is normal to the flow direction (figure 1). For the specified geometry and physical properties, the Lorentz force dominates over the viscous and inertial forces for both plasma and W-melt, since the Hartmann and Stuart numbers are large ($Ha_m \sim 248$, $Ha_p \sim 102$, $N_m \sim 2.6$, $N_p \sim 10^4$ – 10^6). For W-melt, the hydrodynamic Reynolds number is large ($Re_m \sim 10^4$) meaning that the inertial forces dominate over the viscous forces. However, the viscous forces are prevailing over the inertial forces for plasma flow, since the hydrodynamic Reynolds number is small ($Re_p \sim 0.004$ – 0.4). The magnetic Reynolds number is small for both W-melt and plasma ($Rem_m \sim 0.08$, $Rem_p \sim 0.0002$ – 0.02) indicating that the induced magnetic field is negligible compared with the imposed magnetic field.

3.2. Motion of W-melt on a substrate in the absence of plasma effects

First, we study a case when the plasma located above the W-melt layer is considered as motionless (velocity components are $(0, 0, 0) \text{ m s}^{-1}$). The motion of W-melt is investigated on a substrate without the influence of magnetic field ($\vec{B} = (0, 0, 0) \text{ T}$) and when a magnetic field is parallel ($\vec{B} = (5, 0, 0) \text{ T}$) and perpendicular ($\vec{B} = (0, 5, 0) \text{ T}$) to the W-melt surface (figure 2).

At $t = 0$, the velocity of W-melt has components $(2, 0, 0) \text{ m s}^{-1}$. The interface between W-melt and plasma is flat. The volume fraction (alpha) of W-melt is shown in figure 2 for different times. It is observed that in the absence of magnetic field, the running waves with wavelengths $\lambda \sim 400$ – $500 \mu\text{m}$ are developed on the melt surface after $t \sim 40 \text{ ms}$. The steady-state motion of W-melt with wavy surface is shown in figure 2(a) for $t \sim 60 \text{ ms}$. When the externally applied magnetic field of 5 T and W-melt flow are in the same direction, the interface remains flat (figure 2(b)). The development of surface waves is suppressed and they are not observed at long times ($t \sim 150 \text{ ms}$). This is because the flow structures like vortices are affected by the Lorentz force (figure 3). The Lorentz force acts normally on the wave crests smoothing out velocity variations in vortices and suppressing the development

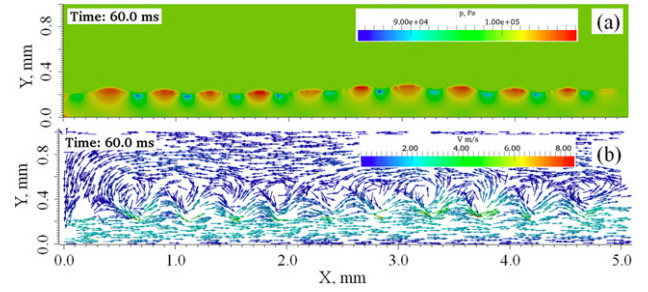


Figure 3. Fields of (a) pressure and (b) velocity of W-melt flow for the case of zero plasma speed and in the absence of magnetic field (figure 2(a)).

of surface waves. Our finding is in excellent agreement with previous theoretical and experimental results on the propagation of surface waves on liquid gallium [57]. It was observed in those studies that surface waves are completely damped when a magnetic field is imposed parallel to the propagation direction of liquid metal [57]. When the magnetic field of 5 T is imposed perpendicularly to the direction of W-melt flow, small-amplitude standing waves are generated after $t \sim 8 \text{ ms}$. These small-amplitude waves on the W-melt surface are illustrated in figure 2(c) at $t \sim 150 \text{ ms}$. In this case the vortex evolution is damped by the Lorentz forces acting against the flow direction. The waves appear suddenly over the entire surface after $\sim 8 \text{ ms}$ and keep oscillating up and down. The timescale of wave development is about 5 times faster compared with that in the absence of magnetic field. In measurements [57], no damping of surface waves was found with a perpendicular magnetic field in the deep liquid metal. However, in our modelling the depth of W-melt is only $\sim 200 \mu\text{m}$, and therefore waves are considerably damped. The pressure and velocity fields of W-melt flow are shown in figure 3 at $t \sim 60 \text{ ms}$. These correspond to the case shown in figure 2(a).

It can be seen that the pressure deviates from background value ($\sim 10^5 \text{ Pa}$) at the W-melt surface (figure 3(a)). The pressure is higher at wave crests and lower at melt troughs. The temperature field behaves similarly, since the temperature of melt and plasma is kept the same. Therefore, temperature fields are not reported in this paper. The vector field of velocity demonstrates vortices at the interface (figure 3(b)). For clarity, the velocity vectors are shown using randomly spaced arrows. The W-melt moves downstream with a velocity $\sim 2 \text{ m s}^{-1}$. The velocity is close to zero on the bottom due to the non-slip boundary condition. Due to vortex development, the plasma is entrained into the motion in the opposite direction. At troughs, the velocity may reach locally up to $\sim 8 \text{ m s}^{-1}$. The vortex structures are not observed at the interface in the presence of a parallel or perpendicular magnetic field (results are not shown).

3.3. Effect of plasma stream on W-melt surface

To study the effect of plasma on the W-melt surface, we performed calculations considering the plasma flowing with velocities of 100 , 1000 and 5000 m s^{-1} . The volume fraction of W-melt at 4 ms is shown in figure 4 in the absence and the presence of magnetic field. The calculation conditions are the same as those of figure 2, but the plasma flows with a speed of 100 m s^{-1} .

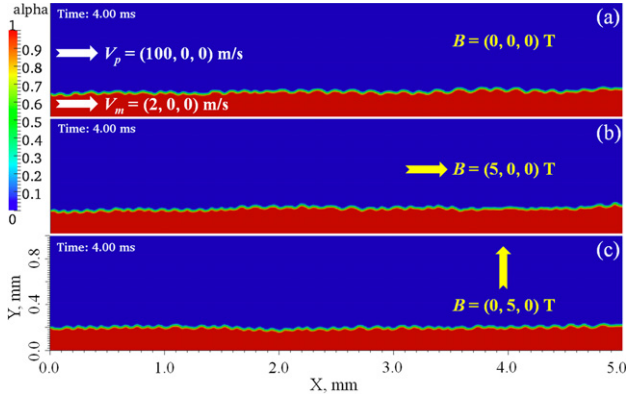


Figure 4. Volume fraction (alpha) of W-melt (a) without magnetic field, (b) with an externally applied magnetic field parallel to the direction of W-melt flow and (c) a magnetic field normal to the direction of W-melt flow. The velocity of W-melt is 2 m s^{-1} . The plasma flows with a velocity of 100 m s^{-1} .

It can be seen that the stream of plasma with a velocity of 100 m s^{-1} flowing over an W-melt layer that is moving with a speed of 2 m s^{-1} generates the surface waves with a wavelength of $\sim 100 \mu\text{m}$ (figure 4(a)). The waves are developed after $\sim 1 \text{ ms}$ on the entire interface. The magnetic field of 5 T that is either parallel or perpendicular to the direction of W-melt motion has insignificant effects on the development and propagation of waves (figures 4(b) and (c)). The flattened portions of the interface are observed for the case of magnetic field of 5 T aligned with the direction of W-melt motion (figure 4(b)). The small-amplitude waves are oscillating and their development is slightly delayed (developed after $\sim 1.4 \text{ ms}$) when the magnetic field of 5 T is perpendicular to the direction of W-melt motion (figure 4(c)). The map of pressure and vector fields of velocity and magnetic field are shown in figure 5 for $t \sim 5 \text{ ms}$. They correspond to the case shown in figure 4(c). These fields of pressure and velocity are similar for other cases shown in figures 4(a) and (b). We can see that the pressure is again uniform ($\sim 10^5 \text{ Pa}$) in the computational domain except the interface where pressure fluctuations are observed (figure 5(a)). However, the distribution of alternating high and low pressure vortices at wave crests and troughs is more compact compared with that of figure 3(a). This is because the wavelength of surface waves is much shorter. The plasma flows with a velocity of $\sim 100 \text{ m s}^{-1}$ (figure 5(b)).

The speed of plasma is varied reaching $\sim 120 \text{ m s}^{-1}$ locally at some places. The thin shear layer is clearly seen at the interface between the plasma and W-melt where the velocity drops from ~ 100 to $\sim 2 \text{ m s}^{-1}$. The flow in the shear layer involves complex vortical structures. The vertical magnetic field of 5 T remains nearly intact (figure 5(c)). The parallel magnetic field corresponding to the case shown in figure 4(b) behaves similarly. There are very small fluctuations of magnetic field at the interface that are negligible (fourth–fifth digit after comma). The reason is that the magnetic Reynolds number is small, and thus the wave-induced magnetic field can be ignored.

The maps of volume fraction of W-melt impacted by a plasma with a speed of 1000 m s^{-1} are shown in figure 6 in the absence of an external magnetic field (figure 6(a)) and in the presence of a horizontal (figure 6(b)) and vertical (figure 6(c))

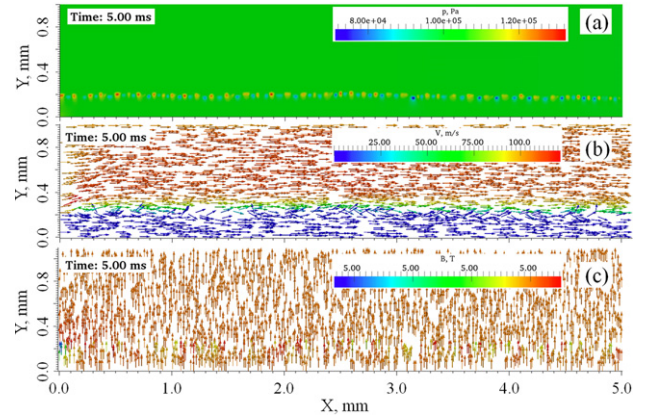


Figure 5. Map of pressure (a) and vector fields of velocity (b) and magnetic field (c) for plasma flowing with a velocity of 100 m s^{-1} in the presence of magnetic field that is perpendicular to W-melt layer (figure 4(c)).

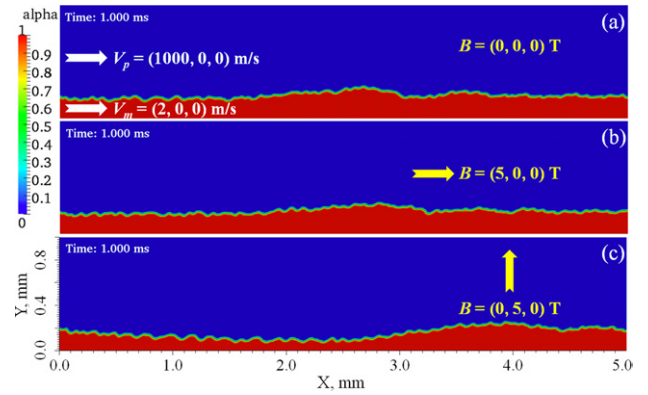


Figure 6. Volume fraction (alpha) of W-melt (a) without magnetic field, (b) with an externally applied magnetic field parallel to the direction of W-melt flow and (c) a magnetic field perpendicular to the direction of W-melt flow. The velocity of W-melt is 2 m s^{-1} . The plasma flows with a velocity of 1000 m s^{-1} .

magnetic field. It is observed that the plasma with a velocity of 1000 m s^{-1} streaming over an W-melt layer moving with a speed of 2 m s^{-1} initially induces a large single wave near the inlet. This large wave with a series of small waves behind it moves forward on the melt interface. It reaches the outlet at time less than $\sim 1 \text{ ms}$. Thus, the surface waves develop much faster at higher plasma speeds (compare figures 4 and 6). The magnetic field of 5 T that is parallel or perpendicular to W-melt does not prevent the development and propagation of surface waves. It is observed that a high-speed flow of plasma significantly thins large portions of melt layer, especially when the magnetic field is perpendicular to the direction of W-melt motion (figure 6(c)). In other regions, the melt thickness is increased. The short waves with a wavelength on the order of $20\text{--}40 \mu\text{m}$ are formed on the surface of W-melt. Thus, the wavelength of surface waves decreases with increasing velocity of plasma stream (compare figures 4 and 6). The fields of pressure, velocity and magnetic field (not shown) behave similarly to those of the plasma flow with a velocity of 100 m s^{-1} (figure 5).

The entrainment of W-melt into the viscous plasma flowing with a speed of 5000 m s^{-1} is shown in figure 7. The

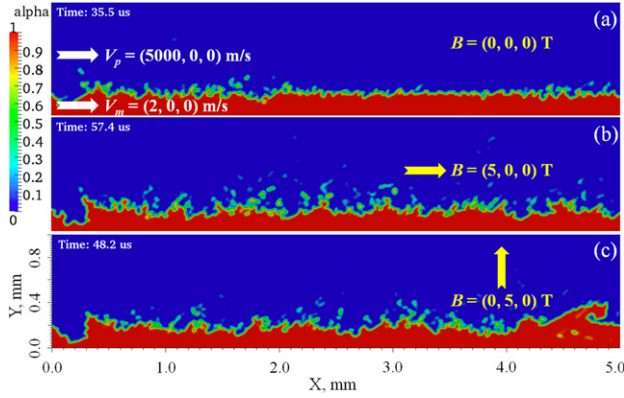


Figure 7. Volume fraction (α) of W-melt (a) without magnetic field, (b) with an externally applied magnetic field parallel to the direction of W-melt flow and (c) a magnetic field perpendicular to the direction of W-melt flow. The velocity of W-melt is 2 m s^{-1} . The plasma flows with a velocity of 5000 m s^{-1} .

growth of short-length waves and formation of droplets is initially observed near the inlet when the stream of viscous plasma with a velocity of 5000 m s^{-1} impacts W-melt layer moving with a speed of 2 m s^{-1} . The development of small ripples and their disintegration into droplets is then occurred on the whole interface of a melt layer within tens of microseconds. Fine droplets are sprayed from the melt and dragged away by the plasma flow. The topology of the W-melt interface becomes very complex (figure 7). The timescales of melt-layer motion as a whole (tens ms, figure 2) and wave development with droplet ejection (tens μs , figure 7) are widely separated. Also, the wavelength of surface waves produced by W-melt motion itself with a velocity of $\sim 2 \text{ m s}^{-1}$ (figure 2) and those generated by high-speed plasma streaming with $0.1\text{--}5 \text{ km s}^{-1}$ is quite different. The horizontal or vertical magnetic field does not suppress droplet ejection and disintegration of melt layer.

The vector fields of velocity are shown in figure 8 for time $t \sim 20 \mu\text{s}$ in the absence (figure 8(a)) and the presence (figures 8(b) and (c)) of a magnetic field. The background velocity of plasma is 5000 m s^{-1} . Shear regions, large vortical and swirling flow structures can be seen in figure 8. At some places, the local velocity of plasma is about 2–3 times higher than the background velocity. The melt is involved into a rotating movement of plasma by virtue of the vortical motion.

At the plasma–melt interface the boundary layer is developed which is highly irregular due to vortical structures. Within this boundary layer, the plasma velocity sharply drops from ~ 5000 to $\sim 2 \text{ m s}^{-1}$. Since the Reynolds number of plasma is small (section 3.1), the viscous plasma forces are very important in the boundary layer. Due to high velocity gradients, the destabilizing viscous stresses can overcome the stabilizing effect of surface tension. Small disturbances on the W-melt surface can grow and develop into fine droplets. These droplets are then entrained and carried away by the plasma flow (figure 7).

3.4. Viscous stability analysis of W-melt layer

The viscous stability analysis [38] based on the viscous potential flow theory [58] was previously developed to study W-melt instability due to the plasma flow. It was predicted

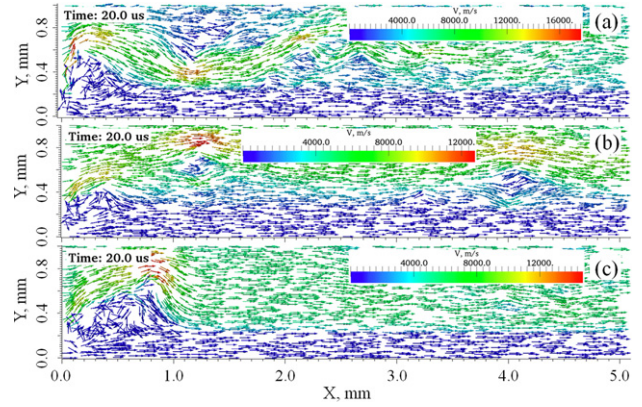


Figure 8. The vector fields of velocity for plasma flowing with 5000 m s^{-1} in (a) the absence of magnetic field, (b) in the presence of parallel magnetic field and (c) in the presence of magnetic field perpendicular to W-melt layer.

that viscous normal stress at the interface has destabilizing effect on melt layers. Here this viscous stability analysis is used to estimate the critical velocity and wavelength for our modelling conditions. The critical velocity and growth rate of surface waves as a function of wavelength λ are shown in figure 9.

The region of instability is located above the curve in figure 9(a). It is seen that unstable waves with wavelengths $\sim 2\text{--}10 \text{ mm}$ can be produced by a plasma flowing with a velocity higher than $\sim 600 \text{ m s}^{-1}$. However, these wavelengths are more than an order of magnitude larger than the thickness of melt layer, $\sim 200 \mu\text{m}$. For a plasma streaming with $\sim 1000 \text{ m s}^{-1}$, the fastest growing wavelength is $\sim 600 \mu\text{m}$. This is about three times larger than the melt thickness. These large waves can be associated with variations of the melt thickness seen in figure 6. The characteristic time of wave growth $\sim 0.2 \text{ ms}$ can be estimated from figure 9(b). These timescales of wave development are observed in the modelling (figure 6). The fastest growing ‘dangerous’ wavelength of surface waves produced by the flow of plasma with a velocity of $\sim 5000 \text{ m s}^{-1}$ is on the order of $\sim 30 \mu\text{m}$ (figure 9(a)). This wavelength is smaller than the thickness of W-melt, and the ejection of droplets is expected from the melt surface. The timescale of droplet development is on the order of $\sim 1 \mu\text{s}$ (figure 9(b)). The droplets are indeed observed in the simulation on this timescale (figure 7).

4. Summary

Melt-layer erosion and splashing of metallic plasma facing components in tokamaks during plasma instabilities is a very serious problem. To predict and simulate the behaviour of tungsten material during plasma disruptions and giant ELMs, comprehensive and integrated VoF-MHD model is developed that combines the Navier–Stokes equations with heat conduction and magnetic induction equations. The modelling of coupled W-melt-plasma flow is performed. The effect of plasma flow speed on the W-melt stability is investigated. In the absence of plasma stream, it is observed that surface waves are developed on flowing W-melt with wavelengths on the order of $\sim 400\text{--}500 \mu\text{m}$. These waves

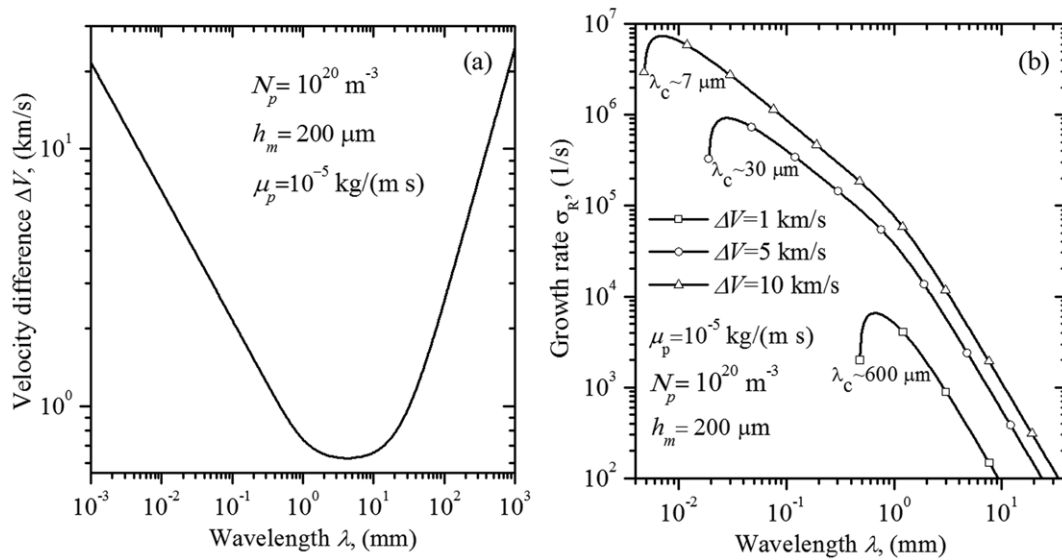


Figure 9. Critical velocity (a) and growth rate (b) of waves on the W-melt surface as a function of wavelength.

are suppressed by the magnetic field of 5 T aligned with the direction of W-melt motion. The small standing waves are observed when the magnetic field of 5 T is perpendicular to the direction of W-melt motion. In the presence of plasma stream, the magnetic field that is either parallel or perpendicular to the W-melt layer does not suppress the development and propagation of surface waves. At high plasma velocity of $\sim 5 \text{ km s}^{-1}$, the growth of small ripples and their disintegration into droplets occurs on the whole surface of W-melt layer within tens of microseconds. It is generally observed that (1) surface waves generated due to W-melt motion itself with $\sim 2 \text{ m s}^{-1}$ and those produced by high-speed plasma flow with $\sim 0.1\text{--}5 \text{ km s}^{-1}$ have different wavelengths; (2) wavelength of surface waves decreases with increasing velocity of plasma stream; (3) surface waves develop much faster at higher plasma speeds; and (4) timescales of melt motion as a whole (tens ms) and droplet ejection (tens μs) are quite different. These effects of plasma on the W-melt motion are present on the typical timescales of ELMs (milliseconds), and therefore they are also valid under steady-state operation conditions. More detail modelling and simulation coupled with well-defined relevant experiments to tokamak conditions are critically needed to fully understand the consequences of melt-layer behaviour and splashing during abnormal plasma events.

Acknowledgment

This work is supported by the US Department of Energy, Office of Fusion Energy Sciences.

References

- [1] Federici G. *et al* 2001 Plasma–material interactions in current tokamaks and their implications for next step fusion reactors *Nucl. Fusion* **41** 1967
- [2] Federici G. 2006 Plasma wall interactions in ITER *Phys. Scr.* **T124** 1
- [3] Hassanein A. and Konkashbaev I. 1999 Comprehensive physical models and simulation package for plasma/material interactions during plasma instabilities *J. Nucl. Mater.* **273** 326
- [4] Hassanein A. *et al* 2009 Integrated simulation of plasma surface interaction during edge localized modes and disruptions: self-consistent approach *J. Nucl. Mater.* **390–91** 777
- [5] Lasner E. and Schubert W.-D. 1999 *Tungsten: Properties, Chemistry, Technology of the Element, Alloys and Chemical Compounds* (New York: Kluwer)
- [6] Hirooka Y. *et al* 1992 Evaluation of tungsten as a plasma-facing material for steady-state magnetic fusion devices *J. Nucl. Mater.* **196** 149
- [7] Wolfer W.G. and Hassanein A.M. 1982 On Melt layer stability following a plasma disruption *J. Nucl. Mater.* **111** 560
- [8] Hassanein A.M. *et al* 1982 Dynamics of melting, evaporation, and resolidification of materials exposed to plasma disruptions *J. Nucl. Mater.* **111** 554
- [9] Hassanein A. and Konkashbaev I. 1996 Lifetime evaluation of plasma-facing materials during a tokamak disruption *J. Nucl. Mater.* **233** 713
- [10] Hassanein A. *et al* 1997 Modeling and simulation of melt-layer erosion during a plasma disruption *J. Nucl. Mater.* **241** 288
- [11] Hassanein A. 2002 Prediction of material erosion and lifetime during major plasma instabilities in tokamak devices *Fusion Eng. Des.* **60** 527
- [12] Bazylev B.N. *et al* 2007 Melt damage simulation of W-macrobrush and divertor gaps after multiple transient events in ITER *J. Nucl. Mater.* **363** 1011
- [13] Bazylev B. *et al* 2008 Behaviour of melted tungsten plasma facing components under ITER-like transient heat loads Simulations and experiments *Fusion Eng. Des.* **83** 1077
- [14] Bazylev B. *et al* 2009 Experimental and theoretical investigation of droplet emission from tungsten melt layer *Fusion Eng. Des.* **84** 441
- [15] Bazylev B. *et al* 2011 Numerical simulations of tungsten melt layer erosion caused by $J \times B$ force at TEXTOR *Phys. Scr.* **T145** 014054
- [16] Sergienko G. *et al* 2007 Erosion of a tungsten limiter under high heat flux in TEXTOR *J. Nucl. Mater.* **363** 96
- [17] Sergienko G. *et al* 2007 Experience with bulk tungsten test-limiters under high heat loads: melting and melt layer propagation *Phys. Scr.* **T128** 81
- [18] Coenen J.W. *et al* 2013 Evolution of surface melt damage, its influence on plasma performance and prospects of recovery *J. Nucl. Mater.* **438** S27

- [19] Litunovsky V.N. *et al* 2000 Material response due to simulated plasma disruption loads *Fusion Eng. Des.* **49–50** 249
- [20] Arkhipov N.I. *et al* 2000 Material erosion and erosion products in disruption simulation experiments at the MK-200 UG facility *Fusion Eng. Des.* **49–50** 151
- [21] Bandura A.N. *et al* 2002 Melt layer behavior of metal targets irradiated by powerful plasma streams *J. Nucl. Mater.* **307** 106
- [22] Tereshin V.I. *et al* 2003 Influence of plasma pressure gradient on melt layer macroscopic erosion of metal targets in disruption simulation experiments *J. Nucl. Mater.* **313** 685
- [23] Federici G. *et al* 2005 Effects of ELMS and disruptions on ITER divertor armour materials *J. Nucl. Mater.* **337** 684
- [24] Garkusha I.E. *et al* 2007 Tungsten melt layer erosion due to $J \times B$ force under conditions relevant to ITER ELMS *J. Nucl. Mater.* **363** 1021
- [25] Garkusha I.E. *et al* 2009 Experimental study of plasma energy transfer and material erosion under ELM-like heat loads *J. Nucl. Mater.* **390–91** 814
- [26] Zhitlukhin A. *et al* 2007 Effects of ELMS on ITER divertor armour materials *J. Nucl. Mater.* **363** 301
- [27] Klimov N. *et al* 2009 Experimental study of PFCs erosion under ITER-like transient loads at plasma gun facility QSPA *J. Nucl. Mater.* **390–91** 721
- [28] De Temmerman G. *et al* 2013 Melt-layer motion and droplet ejection under divertor-relevant plasma conditions *Nucl. Fusion* **53** 023008
- [29] Dale G.E. and Bourham M.A. 1998 Melt layer erosion and resolidification of metallic plasma facing components *17th IEEE/NPSS Symp. on Fusion Engineering* vol 2 p 892
- [30] Wurzh H. *et al* 2001 Macroscopic erosion in tokamak off normal events *Fusion Eng. Des.* **56–57** 397
- [31] Safronov V. *et al* 2001 Material erosion and erosion products under plasma heat loads typical for ITER hard disruptions *J. Nucl. Mater.* **290** 1052
- [32] Coenen J.W. *et al* 2011 Tungsten melt layer motion and splashing on castellated tungsten surfaces at the tokamak TEXTOR *J. Nucl. Mater.* **415** S78
- [33] Coenen J.W. *et al* 2011 Analysis of tungsten melt-layer motion and splashing under tokamak conditions at TEXTOR *Nucl. Fusion* **51** 083008
- [34] Coenen J.W. *et al* 2011 Melt-layer ejection and material changes of three different tungsten materials under high heat-flux conditions in the tokamak edge plasma of TEXTOR *Nucl. Fusion* **51** 113020
- [35] Shi Y. *et al* 2011 Boiling induced macroscopic erosion of plasma facing components in fusion devices *Fusion Eng. Des.* **86** 155
- [36] Miloshevsky G.V. and Hassanein A. 2010 Modelling of Kelvin–Helmholtz instability and splashing of melt layers from plasma-facing components in tokamaks under plasma impact *Nucl. Fusion* **50** 115005
- [37] Shi Y. *et al* 2011 Theoretical studies of macroscopic erosion mechanisms of melt layers developed on plasma facing components *J. Nucl. Mater.* **412** 123
- [38] Miloshevsky G. and Hassanein A. 2013 Splashing and boiling mechanisms of melt layer losses of PFCs during plasma instabilities *J. Nucl. Mater.* **438** S155
- [39] Bazylev B. *et al* 2009 Experimental validation of 3D simulations of tungsten melt erosion under ITER-like transient loads *J. Nucl. Mater.* **390–91** 810
- [40] Miloshevsky G. and Hassanein A. 2011 Modeling of macroscopic melt layer splashing during plasma instabilities *J. Nucl. Mater.* **415** S74
- [41] OpenFOAM (2013), user guide, version 2.2.2 Available from: <http://www.openfoam.org>
- [42] Hirt C.W. and Nichols B.D. 1981 Volume of fluid (Vof) method for the dynamics of free boundaries *J. Comput. Phys.* **39** 201
- [43] Berberovic E. *et al* 2009 Drop impact onto a liquid layer of finite thickness: dynamics of the cavity evolution *Phys. Rev. E* **79** 036306
- [44] Weller H.G. *et al* 1998 A tensorial approach to computational continuum mechanics using object-oriented techniques *Comput. Phys.* **12** 620
- [45] Sergienko G. *et al* 2005 Tungsten melting under high power load in the TEXTOR edge plasma *32nd EPS Conf. on Plasma Physics and Controlled Fusion (Tarragona, Spain)* vol 29C (ECA) P-1.019 (http://epsppd.epfl.ch/Tarragona/pdf/P1_019.pdf)
- [46] Boedo J.A. *et al* 2005 Edge-localized mode dynamics and transport in the scrape-off layer of the DIII-D tokamak *Phys. Plasmas* **12** 072516
- [47] Dojcinovic I.P. 2010 Plasma flow interaction with ITER divertor related surfaces *J. Phys.: Conf. Ser.* **257** 012033
- [48] Tereshin V.I. 1995 Quasi-stationary plasma accelerators (QSPA) and their applications *Plasma Phys. Control. Fusion* **37** A177
- [49] Márquez Damián S. Description and utilization of interFoam multiphase solver. Available at <http://infofich.unl.edu.ar/upload/3be0e16065026527477b4b948c4caa7523c8ea52.pdf>
- [50] Deshpande S.S. *et al* 2012 Evaluating the performance of the two-phase flow solver interFoam *Comput. Sci. Discovery* **5** 014016
- [51] Shercliff J.A. 1953 Steady motion of conducting fluids in pipes under transverse magnetic fields *Proc. Camb. Phil. Soc.* **49** 136
- [52] Hunt J.C.R. 1965 Magnetohydrodynamic flow in rectangular ducts *J. Fluid Mech.* **21** 577
- [53] Klostermann J. *et al* 2013 Numerical simulation of a single rising bubble by VOF with surface compression *Int. J. Numer. Methods Fluids* **71** 960
- [54] Shibasaki Y. *et al* 2010 Computation of a rising bubble in an enclosure filled with liquid metal under vertical magnetic fields *ISIJ Int.* **50** 363
- [55] Ubbink H. 2002 Computational fluid dynamics of dispersed two-phase flows at high phase fractions *PhD Thesis* (London: Imperial College of Science, Technology and Medicine)
- [56] Issa R.I. 1986 Solution of the implicitly discretised fluid flow equations by operator-splitting *J. Comput. Phys.* **62** 40
- [57] Ji H.T. *et al* 2005 Study of small-amplitude magnetohydrodynamic surface waves on liquid metal *Phys. Plasmas* **12** 012102
- [58] Funada T. and Joseph D.D. 2001 Viscous potential flow analysis of Kelvin–Helmholtz instability in a channel *J. Fluid Mech.* **445** 263